2010

100 m and 160 m emission as resolved star–formation rate estimators in M33 (HERM33ES

M Boquien

D Calzetti
University of Massachusetts - Amherst, calzetti@astro.umass.edu

Astronomy & Astrophysics manuscript no. article
May 14, 2010

Letter to the Editor

100 μm and 160 μm emission as resolved star–formation rate estimators in M33 (HERM33ES)⋆

M. Boquien[1], D. Calzetti[1], C. Kramer[2], E. M. Xilouris[3], F. Bertoldi[4], J. Braine[5], C. Buchbender[2], F. Combes[6], F. Israel[7], B. Koribalski[8], S. Lord[9], G. Quintana-Lacaci[2], M. Relaño[10], M. Röllig[11], G. Stacey[12], F. S. Tabatabaei[13], R. P. J. Tilanus[14], F. van der Tak[15], P. van der Werf[7], and S. Verley[16]

(Affiliations can be found after the references)

ABSTRACT

Context. Over the past few years several studies have provided estimates of the SFR (star–formation rate) or the total infrared luminosity from just one infrared band. However these relations are generally derived for entire galaxies, which are known to contain a large scale diffuse emission that is not necessarily related to the latest star–formation episode.
Aims. We provide new relations to estimate the SFR from resolved star–forming regions at 100 μm and 160 μm.
Methods. We select individual star–forming regions in the nearby (840 kpc) galaxy M33. We estimate the SFR combining the emission in Hα and at 24 μm to calibrate the emission at 100 μm and 160 μm as SFR estimators, as mapped with PACS/*Herschel*. The data are obtained in the framework of the HERM33ES open time key project.
Results. There is less emission in the HII regions at 160 μm than at 100 μm. Over a dynamic range of almost 2 dex in Σ_{SFR} we find that the 100 μm emission is a nearly linear estimator of the SFR, whereas that at 160 μm is slightly superlinear.
Conclusions. The behaviour of individual star–forming regions is surprisingly similar to that of entire galaxies. At high Σ_{SFR}, star formation drives the dust temperature, whereas uncertainties and variations in radiation–transfer and dust–heated processes dominate at low Σ_{SFR}. Detailed modelling of both galaxies and individual star forming regions will be needed to interpret similarities and differences between the two and assess the fraction of diffuse emission in galaxies.

Key words. galaxies: individual: M33 – galaxies: spiral – galaxies: infrared – galaxies: star formation

1. Introduction

Star formation is one of the main drivers of galaxy formation and evolution and as such the accuracy of the SFR (star–formation rate) determination is of great importance for deriving the cosmic history of galaxies. Along with the UV and the Hα, the total infrared luminosity is widely used to estimate the SFR. To properly quantify the infrared luminosity a good sampling of the infrared SED (spectral energy distribution) is needed (Dale & Helou 2002; Draine & Li 2007). Over the past few years, many authors have shown that the TIR (total infrared) luminosity, and by extension the SFR (Kennicutt 1998), can also be evaluated from monochromatic emission measures (Takeuchi et al. 2005; Calzetti et al. 2007; Rieke et al. 2009; Calzetti et al. 2010; Boquien et al. 2010, Y. Li et al. 2010, in prep.). However, most relations between the far–infrared luminosity and the SFR are established for entire galaxies. At shorter wavelengths, some relations have been derived from individual star–forming regions (Calzetti et al. 2005; Pérez-González et al. 2006; Calzetti et al. 2007; Relaño et al. 2007). As new deep surveys will become available at wavelengths where most of the energy is emitted, it is prudent to try to understand the relation between the integral emission of a galaxy and that of the individual star forming regions. The physical conditions, such as temperature, abundance and emissivity, of the infrared–emitting dust can vary widely in a galaxy, and so does the significant contribution from evolved stars (Lonsdale Persson & Helou 1987; Sauvage & Thuan 1992; Buat & Xu 1996). Therefore, any scaling relation established from the emission of entire galaxies may not be appropriate when applied to resolved star–forming regions in these same galaxies.

The limited resolution of far–infrared instruments onboard IRAS (Infrared Astronomical Observatory), ISO (Infrared Space Observatory) or even *Spitzer* beyond 60 μm made the study of individual star–forming regions within galaxies difficult. However, the recently launched *Herschel* Space Observatory (Pilbratt et al. 2010) with its unprecedented resolution provides the first opportunity to study the spatially resolved far–infrared dust emission in exquisite detail. Such a fine resolution is of the utmost importance to study the emission of star–forming regions located in nearby galaxies in order to provide insights into the fundamental properties of the dust and to quantify the SFR.

With an inclination of 56° (Regan & Vogel 1994) and a distance of only 840 kpc (Freedman et al. 1991), M33 is one of the closest spiral galaxies. It has been imaged by *Herschel* in the context of the HERM33ES Open Time Key Project (Kramer et al. 2010), providing one of the finest views *Herschel* will ever provide of a spiral galaxy from 100 μm to 500 μm (Kramer et al. 2010; Braine et al. 2010; Verley et al. 2010b).

2. Observations and data reduction

2.1. PACS

The observations provided by PACS (Poglitsch et al. 2010) at 100 μm and 160 μm are presented by Kramer et al. (2010) along

⋆ *Herschel* is an ESA space observatory with science instruments provided by European–led Principal Investigator consortia and with important participation from NASA.

with a detailed description of the data processing pipeline. The observations were carried out on 2010-01-07 in parallel mode with a 20″/s scanning speed for a total of 6.3 hours, through a single scan and a perpendicular cross scan. The frames were first processed to level 1 with HIPE (Ott 2010), the drifts were corrected and were deglitched with the second–order deglitcher with a 6-σ threshold. The maps were produced with photproject mapmaker[1] using a two–step masking technique to preserve the diffuse emission from being affected by the high–pass filter. The total flux of the galaxy is consistent with the measures provided by IRAS and *Spitzer* at 100 μm and 160 μm (Kramer et al. 2010). We present the two maps in Figure 1. The pixel size is 3.2″ at 100 μm and 6.4″ at 160 μm for a spatial resolution of 6.7″×6.9″ at 100 μm and 10.7″×12.1″at 160 μm. The absolute calibration uncertainty is 5% at 100 μm and 10% at 160 μm. The total fluxes of M33 agree to within a few percent with those from ISO (Hippelein et al. 2003) and MIPS. In addition, for all radial averages the PACS 160 flux is within 20% of the MIPS 160 one.

2.2. Hα and Spitzer *MIPS 24 μm*

We used the Hα image presented by Hoopes & Walterbos (2000) that is commonly used in the literature (Tabatabaei et al. 2007; Gardan et al. 2007; Verley et al. 2007, 2009, 2010a). The NII contamination was corrected assuming [NII]/Hα=0.05 in the filter bandpass. We also corrected the fluxes for Galactic foreground extinction using the Cardelli et al. (1989) law, assuming E(B-V)=0.042 from the NASA Extragalactic Database[2].

We used the 24 μm MIPS data presented by Tabatabaei et al. (2007). No further processing was performed on this image.

2.3. Flux measurements

All targeted HII regions flux densities were measured in polygonal apertures using IRAF's polyphot procedure. Each polygon was constructed manually from the PACS 160 μm image and tailored to avoid subtraction artefacts in Hα and background sources in MIPS 24 μm images. Each source was selected to be as compact as possible, taking into account the blending at 160 μm to avoid the mix of several star–forming regions of different ages and properties. The background was calculated measuring the mode of the pixels distribution in an annulus around the aperture. Annulus pixels falling into the aperture of a source were automatically discarded. The inner radius of the annulus ranges from 20″ to 70″ by steps of 10″, which were defined to be larger than the equivalent radius of the aperture: $r = \sqrt{S/\pi}$, where S is the area of the aperture. A scale of 50 pc corresponds to an angular size of 11″. The width of the annulus was set to 12″. Aperture correction was performed for 24 μm data[3] and for the PACS bands[4]. As the apertures are not circular, we applied the method presented in Boquien et al. (2007) using the equivalent radius of the aperture.

As a proxy for the SFR we applied the scaling presented by Calzetti et al. (2007): SFR = $[L(H\alpha) + 0.031L(24)]\times5.35\ 10^{-35}$ in $M_\odot\ yr^{-1}$, where $L(H\alpha)$ is the Hα luminosity in W and, $L(24)$ is defined as νL_ν at 24 μm in W, assuming a Kroupa (2001) IMF (initial mass function) with a constant SFR over 100 Myr.

For an easier use of the SFR estimator we will provide in this article, we subsequently worked in Σ (luminosity surface density) because it is distance–independent, in order to facilitate a comparison with other galaxies. To do so, we divided the luminosity by the area of the polygon measured in kpc^2.

3. Results

3.1. General characteristics of HII regions

We selected a total of 179 HII regions from the 160 μm map. The physical equivalent radius of the extraction apertures ranges from 37 pc to 256 pc, with a median of 99 pc. Σ_{100} ranges from 1.0×10^{33} W kpc^{-2} to 1.0×10^{35} W kpc^{-2} and Σ_{160} from 1.5×10^{33} W kpc^{-2} to 5.2×10^{34} W kpc^{-2}. The typical 1-σ uncertainties are 0.09, 0.06, 0.02, and 0.03 dex in Hα, 24 μm, 100 μm, and 160 μm respectively. Σ_{SFR} (SFR density) ranges from 1.2×10^{-3} $M_\odot$ kpc^{-2} yr^{-1} to 1.5×10^{-1} $M_\odot$ kpc^{-2} yr^{-1}.

The fraction of the total flux enclosed in the 179 apertures compared to the total flux of M33 is 0.40, 0.43, 0.35, and 0.24 in Hα, 24 μm, 100 μm, and 160 μm assuming galaxy–integrated fluxes $F(H\alpha) = 4.03 \times 10^{-13}$ W m^{-2}, $F(24) = 49.4$ Jy (Verley et al. 2007), $F(100) = 1288$ Jy, and $F(160) = 1944$ Jy (Kramer et al. 2010). That so little of the total 160 μm flux associated with the selected HII regions suggests that the large–scale diffuse emission seen at this wavelength may not be directly related to the ongoing massive star–formation, which is consistent with the result of Hinz et al. (2004) for M33, but may be heated by non–ionising B and A stars as observed for instance by Israel et al. (1996) in another galaxy with a similar metallicity, NGC 6822.

3.2. 100 μm and 160 μm as SFR estimators

Being closer to the peak IR emission, the 100 μm promises to yield an accurate SFR indicator for HII regions and star–formation–dominated galaxies. In this respect, the high angular resolution *Herschel* data will be essential to establish the range of applicability and any limitation of this indicator.

First of all Σ_{100} and Σ_{160} are very well correlated with a Spearman correlation coefficient $\rho_{100-160} = 0.92$. This is expected because both bands probe the grey body emission of big grains. It appears that Σ_{100} and Σ_{160} are also well correlated with Σ_{SFR}, with a Spearman correlation coefficient $\rho_{SFR-100} = 0.85$ and $\rho_{SFR-160} = 0.77$.

In Figure 2 we present the fits of Σ_{100} and Σ_{160} versus the estimated Σ_{SFR}. To estimate the relations between the SFR and the PACS emission we fitted a linear relation in log–log using an ordinary least–square technique taking into account uncertainties on both axes.

The best fits for M33 HII regions respectively correspond to

$$\log \Sigma_{SFR} = (0.9938 \pm 0.0244) \log \Sigma_{100} - (35.8520 \pm 0.8304) \quad (1)$$

$$\log \Sigma_{SFR} = (1.1333 \pm 0.0293) \log \Sigma_{160} - (40.4325 \pm 0.9931) \quad (2)$$

The relations have a dispersion around the best fit of 0.22 dex and 0.25 dex. We notice that the 100 μm relation is nearly linear, whereas the 160 μm relation is slightly superlinear. This is similar to what Calzetti et al. (2010) found (Eq. 23), even though individual star–forming regions probe a much smaller range of Σ_{SFR}.

[1] PACS photometer – Prime and Parallel scan mode release note. V.1.2, 23 February 2010.

[2] The NASA/IPAC Extragalactic Database (NED) is operated by the Jet Propulsion Laboratory, California Institute of Technology, under contract with the National Aeronautics and Space Administration.

[3] Following the formula provided in the MIPS instrument handbook.

[4] Following the correction provided in PACS photometer – Prime and Parallel scan mode release note. V.1.2, 23 February 2010.

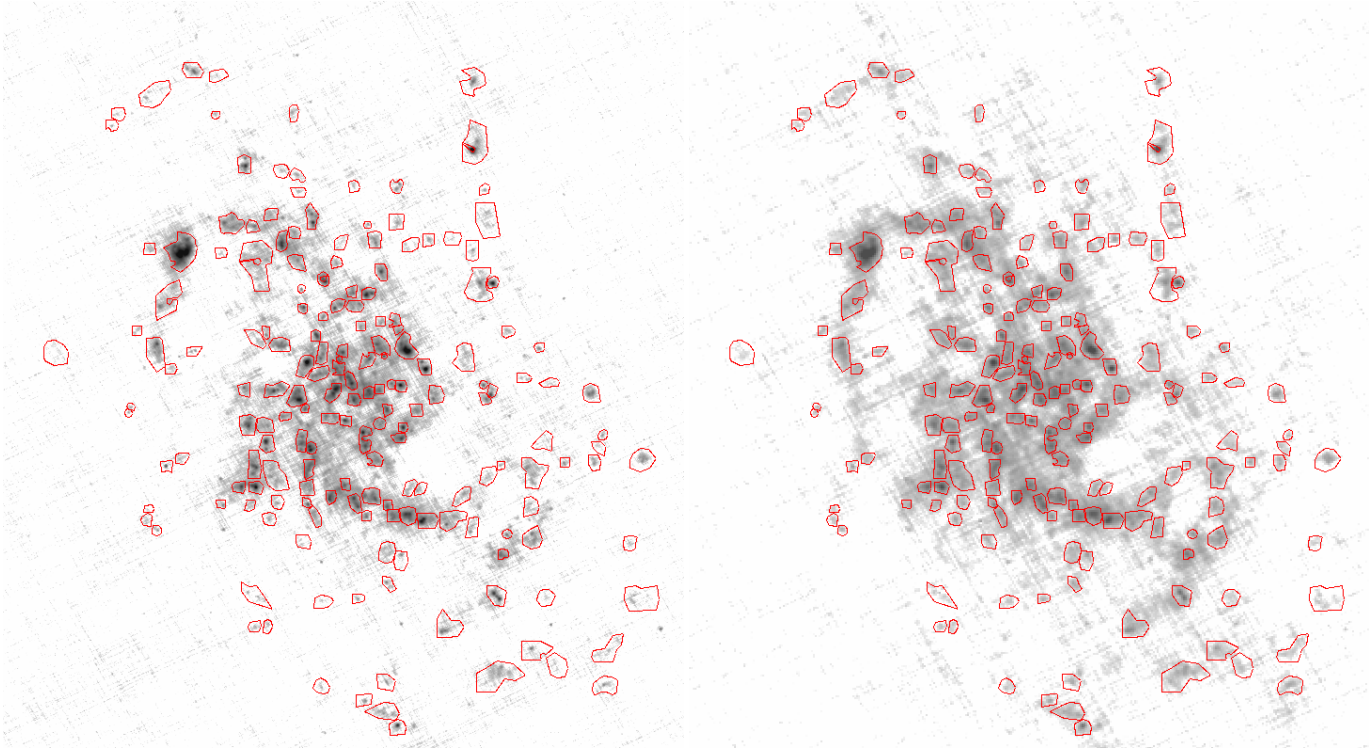

Fig. 1. PACS maps of M33 at 100 μm (left) and 160 μm (right). To probe the full dynamic range of the image a logarithmic scale is used. Individual clumps are well resolved with minimal blending. Some diffuse emission is visible, particularly in the arms and the central region of the galaxy. The visible perpendicular stripes in each scanning direction are sampling artefacts. The red polygons represent the selected apertures. North is up, East is left

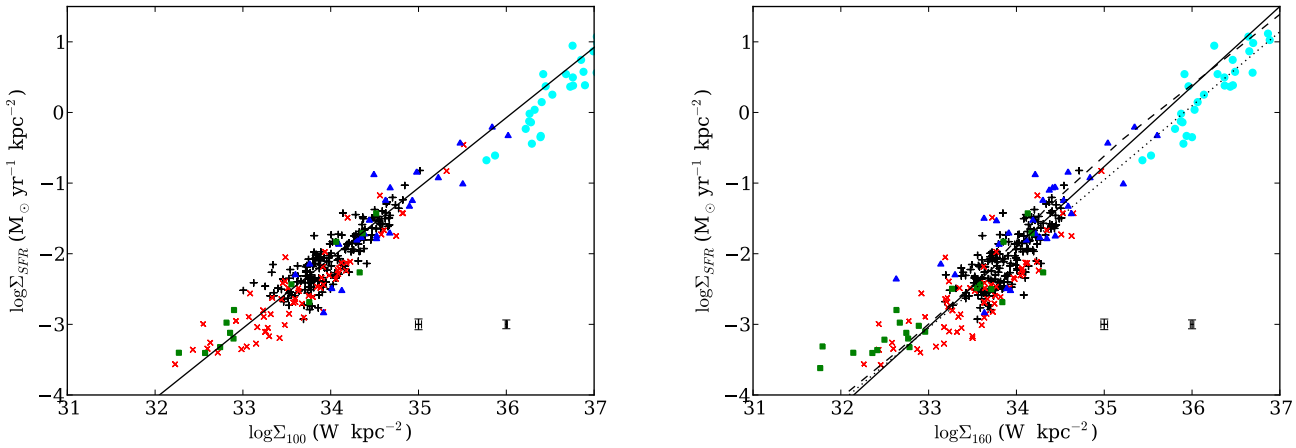

Fig. 2. Σ_{SFR} as a function of Σ_{100} (left) and Σ_{160} (right). A black plus corresponds to individual HII regions in M33. The error bars correspond to the typical uncertainty for the lower and higher 50% percentile. For comparison additional integrated galaxies are also plotted: SINGS (*Spitzer* Infrared Nearby Galaxies Survey, Dale et al. 2007, red crosses), LVL (Local Volume Legacy Survey, Dale et al. 2009, green squares), starburst galaxies from Engelbracht et al. (2008) (blue triangles) and LIRGs from (Luminous Infrared Galaxies Calzetti et al. 2010, cyan circles). These galaxies belong to the high–metallicity bin of Calzetti et al. (2010), which encloses the metallicity of M33 (Magrini et al. 2010). The best fit of selected star–forming regions in M33, taking into account the uncertainties on both axes, is plotted with a solid black line. The dashed line represents the model described in Sect. 4.1 assuming an extinction E(B-V)=0.25, set to reproduce the observed $\Sigma_{H\alpha}/\Sigma_{24}$. Finally the dotted line represents the best fit determined by Calzetti et al. (2010) for entire galaxies.

4. Discussion

4.1. Modeling

To model the individual HII regions we used the Calzetti et al. (2007) model as a baseline. The ionising flux is determined using

Starburst99 (Leitherer et al. 1999) with a Kroupa (2001) IMF, an instantaneous burst and solar metallicity. The extinction is assumed to follow the Calzetti (2001) law. As the $L(H\alpha)/L(24)$ ratio does not show a significant correlation with Σ_{SFR} for our selected regions in M33, we assumed a constant E(B-V)=0.25 mag, set to reproduce the observed mean $\Sigma_{H\alpha}/\Sigma_{24}$. For the dust emissivity we assumed the Draine & Li (2007) model prescriptions for *Spitzer* MIPS 160, pending updated dust emissivities for *Herschel* bands. The model is plotted in Figure 2.

4.2. Comparison with entire galaxies

Calzetti et al. (2010) showed that for entire galaxies the emission at 160 μm correlates linearly with Σ_{SFR}. To compare this with the emission of entire galaxies at 100 μm and 160 μm, we plotted in Figure 2 several samples of relatively metal–rich galaxies from SINGS (*Spitzer* Infrared Nearby Galaxies Survey), LVL (Local Volume Legacy Survey), starburst galaxies from Engelbracht et al. (2008) and some LIRGS (Luminous Infrared Galaxies). Surprisingly, individual star–forming regions and entire galaxies show a similar behaviour. Unfortunately the large scatter in both samples makes any assessment of the contamination by the large diffuse emission in entire galaxies very difficult. However, when they are compared with the relation derived for individual regions, most show a stronger 100 μm and 160 μm emission for a given Σ_{SFR}, especially in the $33 \leq \log \Sigma_x \leq 34.5$ range where x is 100 or 160. Further comparisons to estimate the contamination by a diffuse far–infrared component will require detailed modelling of individual star–forming regions and entire galaxies.

4.3. Dust temperature

The slight non–linearity in the $\Sigma_{160} - \Sigma_{SFR}$ relation hints at a higher dust temperature with increasing Σ_{SFR}, which would have different effects on the two PACS bands because the peak of the emission passes through the filter bandpasses as the temperature increases. Indeed, as dust gets warmer, an increasing fraction will be emitted at shorter wavelengths. In Figure 3 we plot $\Sigma_{160}/\Sigma_{100}$, a proxy for the dust temperature of the warm component, versus the Σ_{SFR}.

We see a clear trend with higher Σ_{SFR} ($\rho = -0.55$) leading to a higher dust temperature. The spanned range is compatible with the emissivity values published by Draine & Li (2007) for $0.5 \leq U \leq 100$, U being the interstellar radiation field normalised to that of the solar neighbourhood. This means that an increasing fraction of the total dust emission is detected in the 100 μm band compared to the 160 μm band. Interestingly we also notice that the trend in entire galaxies is very similar to the trend in individual HII regions in M33 despite the fact that individual regions should have little contamination from the diffuse large scale emission. One possible interpretation is that in both entire galaxies and individual HII regions, star–formation dominates at higher Σ_{SFR} and creates the trend whereas, at lower Σ_{SFR} the trend is influenced by the uncertainties and variations of conditions in the radiation–transfer and dust–heating processes such as the opacity of the star–formation region, the clumpiness of the media, the relative locations of stars and dust clouds, etc.

5. Conclusions

We used the high–resolution *Herschel* 100 μm and 160 μm observations of a nearby star–forming galaxy, M33. We combined

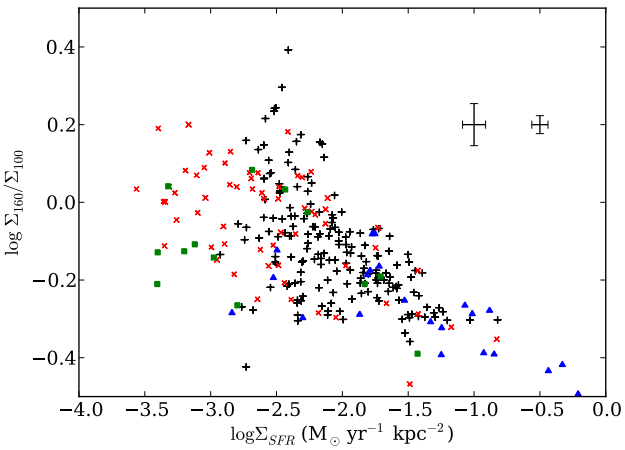

Fig. 3. $\Sigma_{160}/\Sigma_{100}$ vs. Σ_{SFR} (black plusses), for the 179 HII regions selected in M33. The error bars correspond to the typical uncertainty for the lower and higher 50% percentile. For comparison additional entire galaxies are plotted using the same colour scheme as in Fig. 2.

Herschel PACS data with *Spitzer* MIPS 24 μm and ground–based Hα to provide new calibrations of the 100 μm and 160 μm to estimate Σ_{SFR} from individual star–forming regions. For the selected star–forming regions in M33, the 100 μm luminosity is a linear SFR estimator over a factor 100 in surface brightness, whereas the 160 micron luminosity is slightly superlinear. It appears that individual star forming regions exhibit a similar behaviour as entire galaxies taken from the LVL, SINGS, starburst galaxies from Engelbracht et al. (2008) samples when estimating Σ_{SFR} from the 100 μm and 160 μm bands emission. In a similar fashion, the dust temperature – as measured by the ratio of the 160 μm to 100 μm emission – increases as a function of Σ_{SFR}, suggesting that at high Σ_{SFR} the star formation drives the trend for both systems, while at lower Σ_{SFR} uncertainties and variations of conditions in the radiation–transfer and dust–heating processes contribute to the scatter. In other words, the fairly wide dust temperature distribution at low Σ_{SFR} becomes increasingly biased towards higher temperatures at higher Σ_{SFR} in both HII regions and entire galaxies.

Acknowledgements. We thank *Herschel* scientists for their valuable help with the PACS data reduction, in particular Babar Ali, Bruno Altieri, Bidushi Bhattacharya, Nicolas Billot and Marc Sauvage. We also thank the NHSC for providing the computing architecture used in the reduction of the data. We also thank our referee, C. K. Xu, for useful comments that helped improve the quality of this article.

References

Boquien, M., Bendo, G., Calzetti, D., et al. 2010, ApJ, 713, 626
Boquien, M., Duc, P.-A., Braine, J., et al. 2007, A&A, 467, 93
Braine et al., 2010, this volume
Buat, V. & Xu, C. 1996, A&A, 306, 61
Calzetti, D. 2001, PASP, 113, 1449
Calzetti, D., Kennicutt, R. C., Bianchi, L., et al. 2005, ApJ, 633, 871
Calzetti, D., Kennicutt, R. C., Engelbracht, C. W., et al. 2007, ApJ, 666, 870
Calzetti, D., Wu, S., Hong, S., et al. 2010, ApJ, 714, 1256
Cardelli, J. A., Clayton, G. C., & Mathis, J. S. 1989, ApJ, 345, 245
Dale, D. A., Cohen, S. A., Johnson, L. C., et al. 2009, ApJ, 703, 517
Dale, D. A., Gil de Paz, A., Gordon, K. D., et al. 2007, ApJ, 655, 863
Dale, D. A. & Helou, G. 2002, ApJ, 576, 159
Draine, B. T. & Li, A. 2007, ApJ, 657, 810
Engelbracht, C. W., Rieke, G. H., Gordon, K. D., et al. 2008, ApJ, 678, 804
Freedman, W. L., Wilson, C. D., & Madore, B. F. 1991, ApJ, 372, 455

Gardan, E., Braine, J., Schuster, K. F., Brouillet, N., & Sievers, A. 2007, A&A, 473, 91
Hinz, J. L., Rieke, G. H., Gordon, K. D., et al. 2004, ApJS, 154, 259
Hippelein, H., Haas, M., Tuffs, R. J., et al. 2003, A&A, 407, 137
Hoopes, C. G. & Walterbos, R. A. M. 2000, ApJ, 541, 597
Israel, F. P., Bontekoe, T. R., & Kester, D. J. M. 1996, A&A, 308, 723
Kennicutt, Jr., R. C. 1998, ARA&A, 36, 189
Kramer et al., 2010, this volume
Kroupa, P. 2001, MNRAS, 322, 231
Leitherer, C., Schaerer, D., Goldader, J. D., et al. 1999, ApJS, 123, 3
Lonsdale Persson, C. J. & Helou, G. 1987, ApJ, 314, 513
Magrini, L., Stanghellini, L., Corbelli, E., Galli, D., & Villaver, E. 2010, A&A, 512, A63+
Ott, S. 2010, in Astronomical Data Analysis Software and Systems XIX, ed. Y. Mizumoto, K.-I. Morita, and M. Ohishi,, Astronomical Society of the Pacific Conference Series
Pérez-González, P. G., Kennicutt, Jr., R. C., Gordon, K. D., et al. 2006, ApJ, 648, 987
Pilbratt et al., 2010, this volume
Poglitsch et al., 2010, this volume
Regan, M. W. & Vogel, S. N. 1994, ApJ, 434, 536
Relaño, M., Lisenfeld, U., Pérez-González, P. G., Vílchez, J. M., & Battaner, E. 2007, ApJ, 667, L141
Rieke, G. H., Alonso-Herrero, A., Weiner, B. J., et al. 2009, ApJ, 692, 556
Sauvage, M. & Thuan, T. X. 1992, ApJ, 396, L69
Tabatabaei, F. S., Beck, R., Krause, M., et al. 2007, A&A, 466, 509
Takeuchi, T. T., Buat, V., Iglesias-Páramo, J., Boselli, A., & Burgarella, D. 2005, A&A, 432, 423
Verley, S., Corbelli, E., Giovanardi, C., & Hunt, L. K. 2009, A&A, 493, 453
Verley, S., Corbelli, E., Giovanardi, C., & Hunt, L. K. 2010, A&A, 510, A64+
Verley, S., Hunt, L. K., Corbelli, E., & Giovanardi, C. 2007, A&A, 476, 1161
Verley et al., 2010b, this volume

[1] University of Massachusetts, Department of Astronomy, LGRT-B 619E, Amherst, MA 01003, USA e-mail: boquien@astro.umass.edu
[2] Instituto Radioastronomia Milimetrica, Av. Divina Pastora 7, Nucleo Central, E-18012 Granada, Spain
[3] Institute of Astronomy and Astrophysics, National Observatory of Athens, P. Penteli, 15236 Athens, Greece
[4] Argelander Institut für Astronomie. Auf dem Hügel 71, D-53121 Bonn, Germany
[5] Laboratoire d'Astrophysique de Bordeaux, Université Bordeaux 1, Observatoire de Bordeaux, OASU, UMR 5804, CNRS/INSU, B.P. 89, Floirac F-33270, France
[6] Observatoire de Paris, LERMA, 61 Av. de l'Observatoire, 75014 Paris, France
[7] Leiden Observatory, Leiden University, PO Box 9513, NL 2300 RA Leiden, The Netherlands
[8] ATNF, CSIRO, PO Box 76, Epping, NSW 1710, Australia
[9] IPAC, MS 100-22 California Institute of Technology, Pasadena, CA 91125, USA
[10] Institute of Astronomy, University of Cambridge, Madingley Road, Cambridge CB3 0HA, England
[11] KOSMA, I. Physikalisches Institut, Universität zu Köln, Zülpicher Straße 77, D-50937 Köln, Germany
[12] Department of Astronomy, Cornell University, Ithaca, NY 14853, USA
[13] Max Planck Institut für Radioastronomie, Auf dem Hügel 69, D-53121 Bonn, Germany
[14] JAC, 660 North A'ohoku Place, University Park, Hilo, HI 96720, USA
[15] SRON Netherlands Institute for Space Research, Landleven 12, 9747 AD Groningen, The Netherlands
[16] Dept. Física Teórica y del Cosmos, Universidad de Granada, Spain